Monthly Notices of the ROYAL ASTRONOMICAL SOCIETY

MNRAS **528,** 2643–2652 (2024) https://doi.org/10.1093/mnras/stae243
Advance Access publication 2024 January 24

Uncovering the formation of the counter-rotating stellar discs in SDSS J074834.64+444117.8

Min Bao [1,2,3] Yanmei Chen [1,2,3]★ Meng Yang [4]★ Ling Zhu [4] Yong Shi [1,2,3] and Qiusheng Gu [1,2,3]

[1] *School of Astronomy and Space Science, Nanjing University, Nanjing 210023, China*
[2] *Key Laboratory of Modern Astronomy and Astrophysics (Nanjing University), Ministry of Education, Nanjing 210023, China*
[3] *Collaborative Innovation Center of Modern Astronomy and Space Exploration, Nanjing 210023, China*
[4] *Shanghai Astronomical Observatory, Chinese Academy of Sciences, 80 Nandan Road, Shanghai 200030, China*

Accepted 2024 January 19. Received 2024 January 4; in original form 2023 September 25

ABSTRACT

Using the integral field spectroscopic data from Mapping Nearby Galaxies at Apache Point Observatory survey, we study the kinematics and stellar population properties of the two counter-rotating stellar discs in a nearby galaxy SDSS J074834.64+444117.8. We disentangle the two stellar discs by three methods, including Ca II λ8542 double Gaussian fit, penalized pixel fitting (pPXF) spectral decomposition, and orbit-based dynamical model. These three different methods give consistent stellar kinematics. The pPXF spectral decomposition provides the spectra of two stellar discs, with one being more luminous across the whole galaxy named primary disc, and the other named secondary disc. The primary disc is counter-rotating with ionized gas, while the secondary disc is co-rotating with ionized gas. The secondary disc has younger stellar population and poorer stellar metallicity than the primary disc. We estimate the stellar mass ratio between the primary and secondary discs to be ∼5.2. The DESI *g*, *r*, *z* colour image does not show any merger remnant feature in this galaxy. These findings support a scenario that the counter-rotating stellar discs in SDSS J074834.64+444117.8 formed through gas accretion from the cosmic web or a gas-rich companion.

Key words: galaxies: individual: SDSS J074834.64+444117.8 – galaxies: kinematics and dynamics.

1 INTRODUCTION

Counter-rotating stellar discs (CRDs) are characterized by the presence of two stellar discs that are co-spatial in one galaxy but rotating in opposite directions. Such a feature was first discovered in NGC 4550 by absorption line analyses (Rix et al. 1992; Rubin, Graham & Kenney 1992). Moreover, 2σ feature was proposed by Krajnović et al. (2011) to describe the observation of off-centre but symmetric peaks along the major axis in the stellar velocity dispersion field of a galaxy with CRDs, where the co-existing blueshifted and redshifted absorption components contribute to the broadening of absorption lines.

Individual galaxies hosting CRDs have been studied, including NGC 5719 (Coccato et al. 2011), NGC 4550 (Johnston et al. 2013), NGC 3593 (Coccato et al. 2013), NGC 4138 (Pizzella et al. 2014), NGC 448 (Katkov et al. 2016), NGC 5102 (Mitzkus, Cappellari & Walcher 2017), and IC 719 (Pizzella et al. 2018). Using the spectral decomposition method, it is possible to disentangle the properties of the co-spatial stellar discs. Johnston et al. (2013) decomposed the spectra along the major axis of S0 galaxy NGC 4550, finding that the stellar disc that co-rotates with the gas disc has younger stellar population than the counter-rotating one, which indicates the co-rotating stellar disc lately forming from the accreted gas. Coccato et al. (2011) applied the decomposition method to the spectra of spiral galaxy NGC 5719, and revealed that the co-rotating stellar disc not only has younger stellar population, but also has poorer stellar metallicity. Considering that NGC 5719 is interacting with a companion NGC 5713, Coccato et al. (2011) suggested these findings as the accreted gas fuelling the *in situ* formation of a new stellar disc.

With the development of integral field spectroscopic (IFS) surveys, studies on samples of CRDs became feasible, which revealed the dependence of formation scenarios on numerous physical factors. Bevacqua, Cappellari & Pellegrini (2022) selected 64 galaxies with CRDs from ∼4000 galaxies in the MaNGA survey Data Release 16, and found that in most cases the younger stellar disc co-rotates with the gas disc, which supported the formation scenario of gas accretion. However, the gas co-rotates with the older stellar disc in two galaxies, which implies a disc galaxy merging with a gas-poor galaxy with younger stellar population in a retrograde orbit. Moreover, Bao et al. (2022) collected a sample of 101 galaxies with CRDs from 9456 galaxies in the MaNGA survey Product Launch 10, divided the sample into four types based on the stellar and gas kinematics, and proposed different formation scenarios for different types. They suggested that the key factors in the formation of CRDs are the abundance of pre-existing gas in the progenitor and the efficiency of angular momentum consumption between the pre-existing and external gas. Given the complexity of formation mechanisms, it is necessary to adopt reliable methods to disentangle two stellar discs, and compare properties between them as completely as possible to uncover the formation of CRDs.

★ E-mail: chenym@nju.edu.cn (YC); myang@shao.ac.cn (MY)

Orbit-based dynamical model provides a physical method to quantify the structure and dynamics of different galaxy components based on their orbit structure distribution. This method has been applied to galaxies to explore the relation between galaxy components and galaxy assembly history in several IFS survey, such as CALIFA (Zhu et al. 2018b), MaNGA (Jin et al. 2020), SAMI (Santucci et al. 2022), and MUSE (Ding et al. 2023). And the method has recently been updated to include bar properly (Tahmasebzadeh et al. 2022). However, it has not been applied to the galaxies with CRDs, since the line-of-sight velocity distribution (LOSVD) of these galaxies cannot be well described by the widely used Gaussian–Hermite expansion of single dynamical component (Rubino et al. 2021). The solution to this problem relies on the non-parametric LOSVDs which capture the multiple dynamical components (e.g. Katkov et al. 2011; Falcón-Barroso & Martig 2021), providing a new prospect of modelling CRDs with orbit-based dynamical models and public DYNAMITE package (van den Bosch et al. 2008; Jethwa et al. 2020; Thater et al. 2022).

In this paper, we focus on a nearby ($z \sim 0.02$) galaxy SDSS J074834.64+444117.8 (hereafter SDSS J0748+4441). We disentangle the two stellar discs by three methods, including Ca II λ8542 double Gaussian fit, penalized pixel fitting (pPXF) spectral decomposition, and orbit-based dynamical model. The involved data are presented in Section 2. The spatially resolved galaxy parameters, the disentangle results, and the properties of the two stellar discs are presented in Section 3. Finally, we discuss the formation scenario for CRDs in Section 4.

2 THE DATA

MaNGA is an IFS survey conducted as a part of the fourth-generation Sloan Digital Sky Survey (SDSS-IV; Bundy et al. 2015; Law et al. 2016). MaNGA survey provides a representative sample of 10 010 unique galaxies with a flat stellar mass distribution in the range of 10^9–$10^{11}\,M_\odot$ and redshift in the range of $0.01 < z < 0.15$ (Blanton et al. 2017). This survey utilizes the Baryon Oscillation Spectroscopic Survey (BOSS) spectrographs (Smee et al. 2013) on the 2.5-m Sloan Foundation Telescope (Gunn et al. 2006). The dual-channel BOSS spectrographs (Smee et al. 2013) provide simultaneous wavelength coverage from 3600 to 10 000 Å.

For each target, the MaNGA Data Reduction Pipeline (DRP; Law et al. 2016) produced sky-subtracted spectrophotometrically calibrated spectra, and generated three-dimensional data cube containing spatially resolved spectra. The wavelength calibration of the MaNGA data is accurate to 5 km s^{-1} (rms), with a median spectral resolution of 72 km s^{-1} ($R \sim$2000). Moreover, the MaNGA Data Analysis Pipeline (DAP; Westfall et al. 2019) provided measurements with pixel size of 0.5 arcsec spaxel^{-1} ($\sim$211 pc spaxel^{-1}), including stellar kinematics, ionized gas kinematics, emission-line flux, and equivalent width (EQW), as well as spectral indices such as 4000 Å break indicating the light-weighted stellar population age. The gas kinematics in this paper is traced by H α emission, while all the emission-line centres are tied together in the velocity space in MaNGA DAP. Besides, we extract the stellar mass in each spaxel from PIPE3D (Sánchez et al. 2016), which used a spectral fitting tool FIT3D to analyse the physical properties of stellar populations of a galaxy.

SDSS J0748+4441 was chosen from a sample of 101 galaxies hosting CRDs (Bao et al. 2022) since two distinguishable absorption components are clearly shown in one of the Ca II triplet lines at λ8542 which is free from skylines. The MaNGA spectra have high enough signal-to-noise ratio (SNR) for disentangling the absorptions of two stellar discs even on the outskirts ($\sim$1.5 *Re*). The SDSS *g*, *r*, *i* colour image of this galaxy is displayed in Fig. 1(a). The global stellar mass ($M_\star$) and attenuation-corrected star formation rate (SFR) from the MaNGA DRP and DAP indicate that SDSS J0748+4441 locates at the green-valley region.

3 THE RESULTS

3.1 Spatially resolved properties

Fig. 1 displays the kinematics of stars and ionized gas in SDSS J0748+4441. Figs 1(b) and 1(c) display the stellar velocity and velocity dispersion fields for spaxels with median spectral SNR per spaxel higher than 3, where the black dashed line shows the photometric major axis (hereafter major axis). The two black stars in Fig. 1(c) mark the 2σ peaks along the major axis, where the maximum stellar velocity dispersion locates. The presence of two regions with enhanced stellar velocity dispersion along the major axis originates from the existence of two CRDs. Meanwhile, the stellar velocity field in Fig. 1(b) following a regular pattern indicates that it is dominated by the more luminous stellar disc across the whole galaxy.

Figs 1(e) and (f) display the ionized gas velocity and velocity dispersion fields for spaxels with H α emission-line SNR higher than 3. The gas is regularly rotating as displayed in Fig. 1(e), with low gas velocity dispersion around the 2σ peaks (black stars) in Fig. 1(f). We fit the gas velocity field using the KINEMETRY package (Krajnović et al. 2006) to derive the kinematic major axis, which is shown by the grey dashed lines in Figs 1(e) and (f). Combining the stellar and gas velocity fields in Figs 1(b) and (e), we conclude that the more luminous stellar disc and the gas disc in SDSS J0748+4441 are counter-rotating. Referring to the kinematic classification in Bao et al. (2022), this galaxy belongs to Type 2b, where the old stellar disc outshines the newly formed one and counter-rotates with gas disc. In Section 3.2, we will disentangle and compare the properties of two stellar discs.

Fig. 2(a) displays a map of stellar mass surface density ($\Sigma_\star$), for spaxels with median spectral SNR per spaxel higher than 3. The $\Sigma_\star$ is defined as the stellar mass of each spaxel divided by the physical size of the spaxel. Fig. 2(b) displays $\Sigma_\star$ as a function of radius along major axis. $\Sigma_\star$ monotonically decreases with increasing radius, but the gradients in the central region and on the outskirts are obviously different. The grey area with $|R| \leq 2.8$ arcsec separates the central region with high surface density from the outskirts with low surface density. We fit two Gaussian functions to the data points inside and outside the grey area. The blue solid profile shows the Gaussian model for the $\Sigma_\star$ gradient with $|R| \leq 2.8$ arcsec, while the blue dashed profile shows the Gaussian model for the data points with $|R| > 2.8$ arcsec. It is clear that the central region and outskirts follow different $\Sigma_\star$ distributions, dominated by bulge and disc, respectively. We mark a red dashed ellipse with a half major axis of $|R| = 2.8$ arcsec on the $\Sigma_\star$ map, which basically covers the densest bulge region.

Mapping diagnostic emission-line ratios across a galaxy gives the information on the ionization state distribution of gas. Fig. 3(a) displays the [N II] BPT diagram (Baldwin, Phillips & Terlevich 1981) for spaxels with H β, [O III]λ5007, H α, and [N II]λ6583 emission-line SNRs higher than 3. The black solid curve separates the star-forming and composite regions (Kauffmann et al. 2003), while the black dashed curve is the demarcation between the composite and active galactic nucleus (AGN) regions (Kewley et al. 2001). The dots show the line ratios measured in different spaxels, and they are colour-coded by the distances of corresponding spaxels to the black solid curve. Fig. 3(b) displays the spatially resolved BPT diagram,

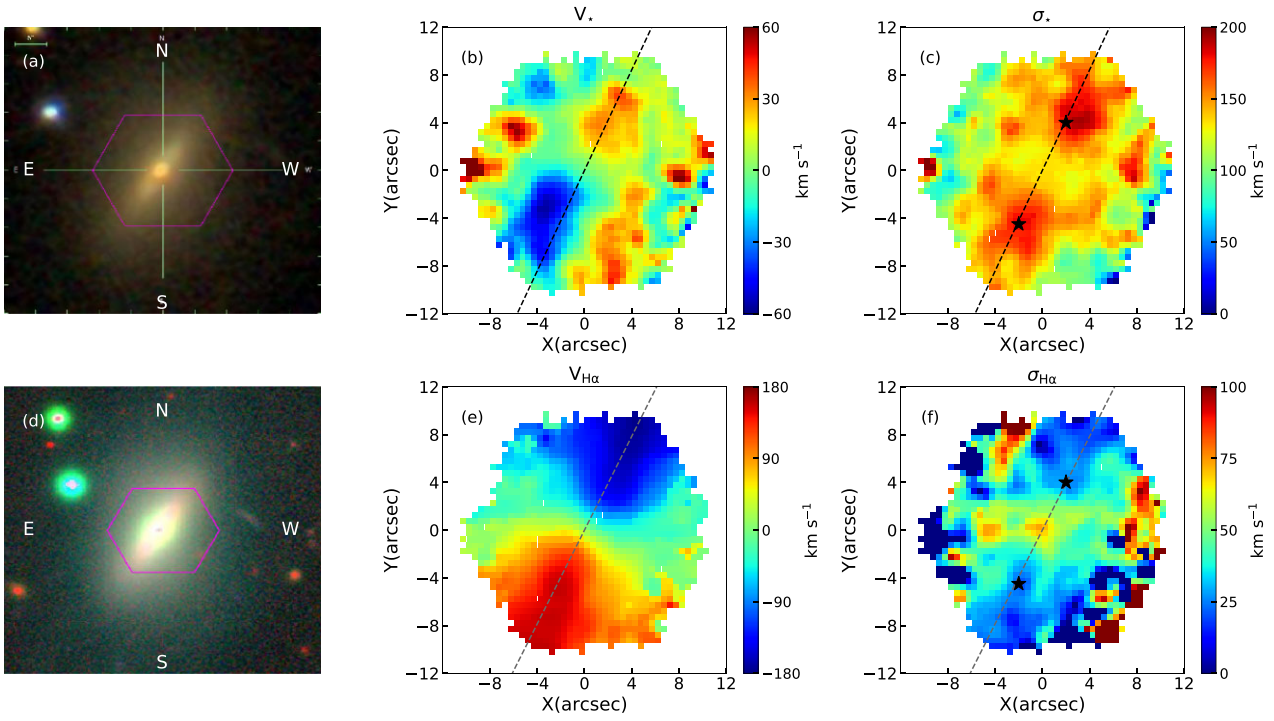

Figure 1. Images and spatially resolved kinematics. (a) SDSS *g*, *r*, *i* colour image. (b) and (c) Stellar velocity and velocity dispersion fields for spaxels with median spectral SNR per spaxel higher than 3. The black dashed lines show the photometric major axis in Figs 1–4. The black stars mark the 2σ peaks along the major axis in Figs 1 and 3. (d) DESI *g*, *r*, *z* colour image. (e) and (f) Gas velocity and velocity dispersion fields for spaxels with Hα emission-line SNR higher than 3. The grey dashed line shows the kinematic major axis.

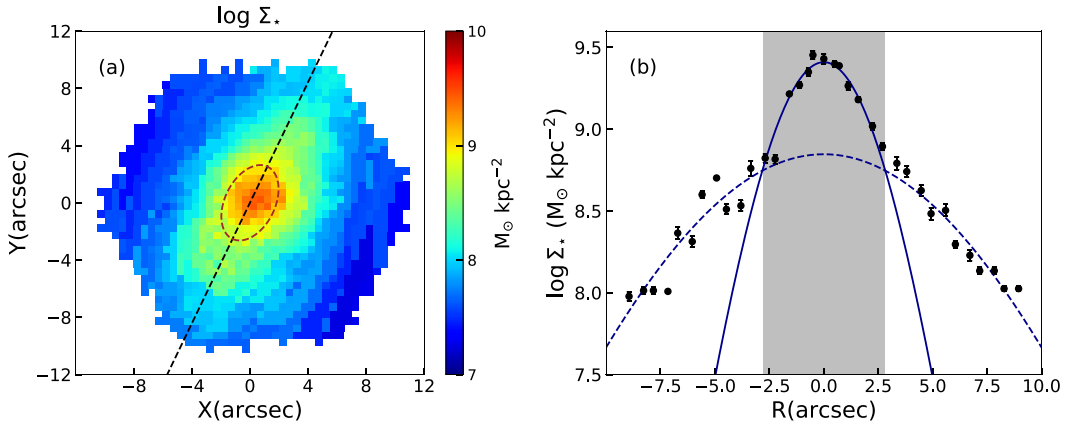

Figure 2. Spatially resolved stellar mass surface density. (a) A map of stellar mass surface density for spaxels with median spectral SNR per spaxel higher than 3. The red dashed ellipse with a half major axis of $|R| = 2.8$ arcsec outlines the bulge region in Figs 2 and 3. (b) The black circles represent the stellar mass surface density at different radii along the major axis. The black vertical bar shows the stellar mass surface density $\pm 1\sigma$ error at each radius. The grey area marks the bulge region with $|R| \leq 2.8$ arcsec in Figs 2, 5, 9, and 10. The blue solid profile shows the Gaussian model for the data points inside the grey area. The blue dashed profile shows the Gaussian model for the data points outside the grey area.

where the colour-codes are the same as Fig. 3(a). The overplotted red dashed ellipse is the same as that in Fig. 2(a) with a half major axis of $|R| = 2.8$ arcsec. Regions inside the ellipse are dominated by AGNs, while the outer regions including the 2σ peaks (black stars) are dominated by star formation.

The SFR describes the ongoing activity of star formation that occurred within the last 10^{6-7} yr. We derive the global SFR of SDSS J0748+4441, which is $\sim 6.7 \times 10^{-2}$ $M_\odot$ yr^{-1}, based on attenuation-corrected Hα flux from MaNGA DAP. Fig. 3(c) displays a map of Hα EQW, which is a good indicator of the specific SFR in the star-forming region. The black contours in Fig. 3(c) outline three regions with enhanced Hα EQW, which are also marked in Fig. 3(b). It is clear that the Hα EQW enhanced regions are dominated by star formation, indicating a higher sSFR in these areas. It is interesting that the two black stars marking the 2σ peaks locate within the contours with the enhanced Hα EQW.

Fig. 3(d) displays a map of 4000 Å break (D_n4000), which is influenced by the intensity of star formation in Gyr-time-scale. Along

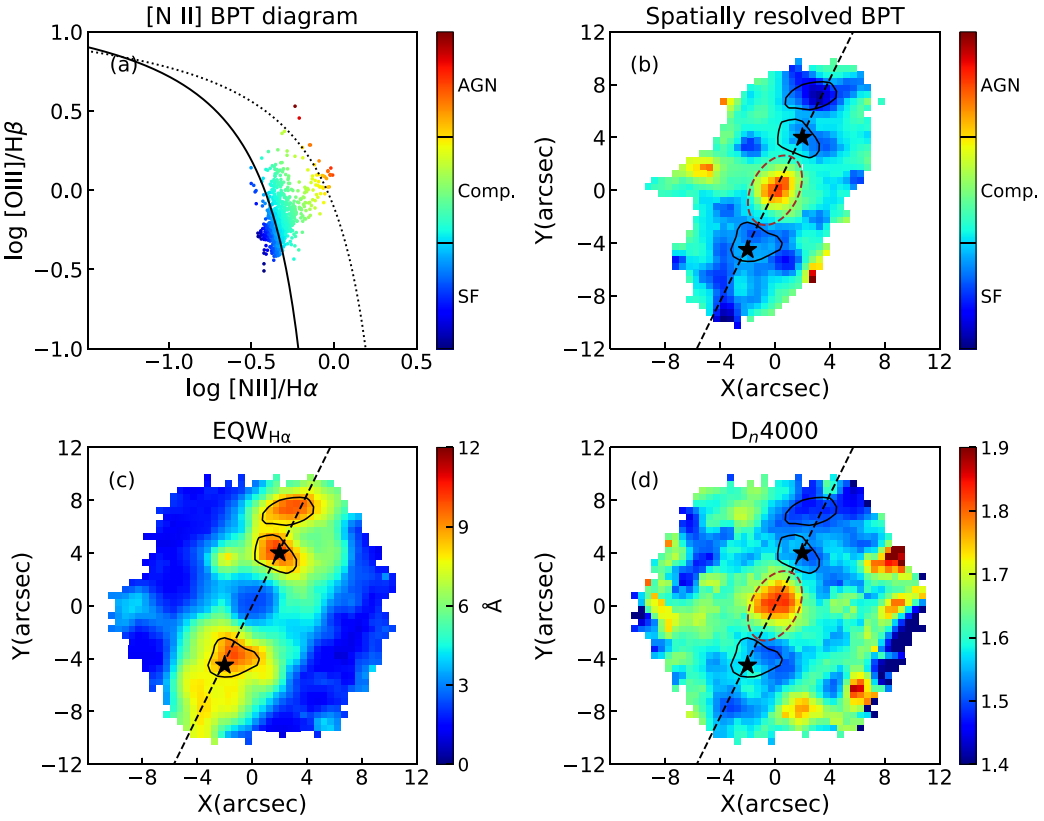

Figure 3. BPT diagrams and spatially resolved properties. (a) [N II] BPT diagram. All the spaxels satisfy the H β, [O III]λ5007, H α, and [N II]λ6583 emission-line SNRs higher than 3. The black solid curve shows the demarcation between the star-forming and composite regions (Kauffmann et al. 2003), while the black dotted curve shows the demarcation between the composite and AGN regions (Kewley et al. 2001). The dots show the line ratios measured in different spaxels, and they are colour-coded by the distances of corresponding spaxels to the black solid curve. (b) Spatially resolved BPT diagram. The SNR criteria and colour-code are the same as panel (a). (c) A map of H α EQW for spaxels with H α emission-line SNR higher than 3. The black contours outline the regions with enhanced H α EQW in panels (c) and (d). (d) A map of 4000 Å break (D$_n$4000) with median spectral SNR per spaxel higher than 3.

the major axis, D$_n$4000 presents the highest value of ∼1.8 in the bulge region (inside the red dashed ellipse), while it has a value of ∼1.5 in the disc region, including the 2σ peaks (black stars) and the enhanced H α EQW regions (black contours). The homologous D$_n$4000 distribution but clumpy H α EQW enhancement in the disc region can be explained by the different star formation time-scales represented by H α emission and D$_n$4000.

3.2 Disentangling two stellar discs

3.2.1 Double Gaussian fit on Ca II λ8542

SDSS J0748+4441 shows obvious asymmetric absorption structure in one of the Ca II triplet lines at λ8542, which provides us an opportunity to disentangle the two stellar discs without model dependence. The other two of Ca II triplet lines at λλ8498, 8662 are contaminated by the skylines.

Fig. 4(a) displays the stellar velocity dispersion field given by MaNGA DAP, in which the two black rings outline the regions around the 2σ peaks (black stars), with the top one named 'Region A' and the bottom one named 'Region B'. To intuitively display the two absorption components in the Ca II λ8542 absorption line, we extract and stack the spectra within Regions A and B, respectively. The Ca II λ8542 absorption lines in the stacked spectra of Regions A and B are shown in the Figs 4(b) and (c), where we use the python-based tool CURVE_FIT to conduct double Gaussian fit on them. The Gaussian models with stronger absorption are in red, the Gaussian models with weaker absorption are in blue, and the best-fitting models are in green which is the combination of blue and red components.

3.2.2 pPXF spectral decomposition

Taking advantage of the different velocities and velocity dispersions of two CRDs, we decompose their contributions to the observed spectrum in each spaxel along the major axis, using the PPXF (Cappellari 2017) code. The code builds two synthetic templates (one for each stellar disc) as linear combination of stellar spectra from the MILES library convolves the templates with two Gaussian LOSVDs with different velocities and velocity dispersions, and ensures the combination of two convolved templates fitted to the observed spectrum by χ^2 minimization.

Fig. 4(d) displays an example of pPXF two kinematic component fit. The observed spectrum shown in black is extracted from the spaxel marked by the black filled star in Fig. 4(a). The red and blue spectra show the optimal models for the two stellar discs. The red spectrum corresponds to the stellar disc with higher flux (hereafter primary disc), and the blue spectrum corresponds to the stellar disc with lower flux (hereafter secondary disc). The green spectrum is the combination of the primary and secondary components; it is our best-fitting model. The insert drawing of Fig. 4(d) highlights the

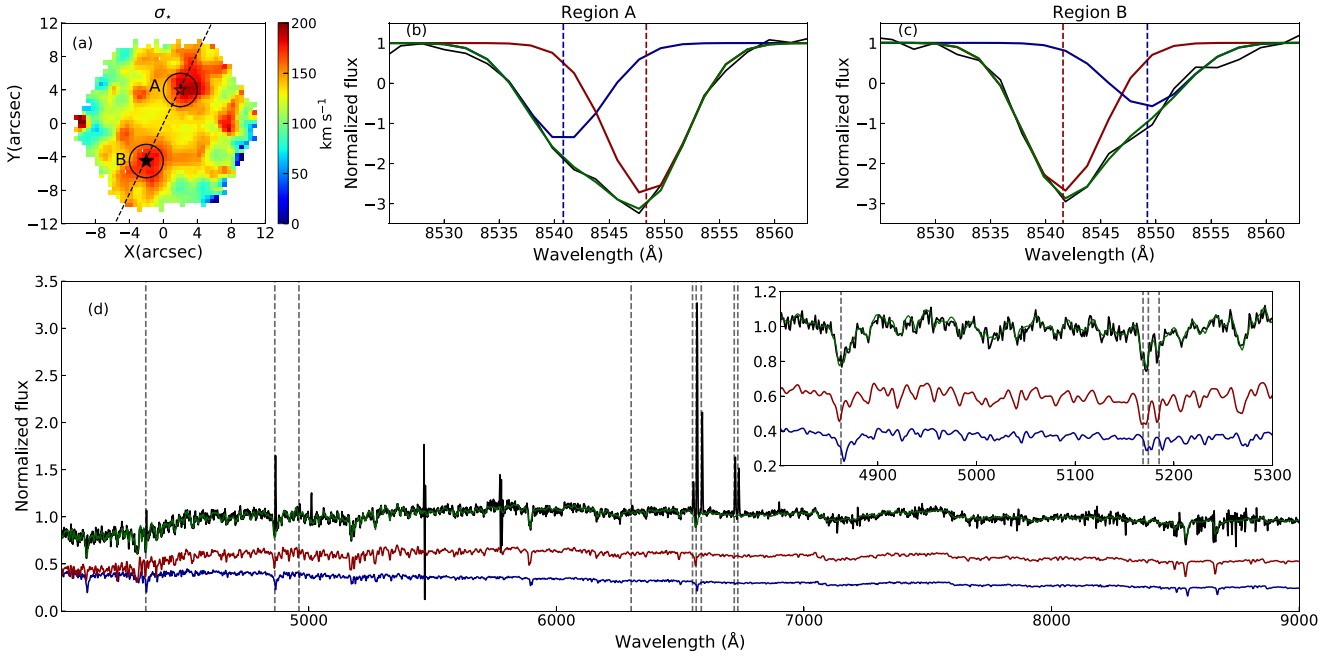

Figure 4. Spectral decomposition. (a) Stellar velocity dispersion field with median spectral SNR per spaxel higher than 3. The black empty and filled stars mark the 2σ peaks. Two black rings outline the regions around the 2σ peaks, with the top one named 'Region A' and the bottom one named 'Region B'. (b) and (c) The black profiles show the stacked Ca II λ8542 lines within Regions A and B, respectively. The red and blue profiles show the double Gaussian fit on the Ca II λ8542 lines, with the stronger absorption in red and weaker absorption in blue. The red and blue dashed lines mark the line centres for corresponding models. The green profiles show the best-fitting models as a combination of red and blue components. (d) The black profile shows the observed spectrum extracted from the filled star in panel (a). The grey dashed lines mark the rest-frame wavelength of emission lines that are masked prior to fit. The red and blue profiles show the two optimal models obtained by the pPXF two kinematic component fit, with primary and secondary discs in red and blue, respectively. The green profile is the best-fitting model as a combination of two models. The insert drawing highlights the spectrum with 4800–5300 Å wavelength range. The four grey dashed lines mark the rest-frame wavelength of H β and Mg I triplet lines.

spectra in [4800, 5300] Å wavelength range. The four grey dashed lines mark the rest-frame wavelength of H β and Mg I triplet lines, where all the absorption profiles are well fitted.

Fig. 5 displays the line-of-sight velocities of stars and gas as functions of radii. The line-of-sight velocities of the two stellar discs are obtained by the pPXF two kinematic component fit on the continuum and absorption lines for spaxels along the major axis. The red and blue circles in Fig. 5 represent the line-of-sight velocities of the primary and secondary discs, respectively. The line-of-sight velocity of the primary disc is overall lower than that of the secondary disc. We also obtain stellar velocity dispersion by the pPXF two kinematic component fit. The stellar velocity dispersions of both primary and secondary discs follow flat distribution along the major axis, with comparable values of 84 and 79 km s^{-1}, respectively. The grey area marks the bulge region, where the stellar kinematics of primary disc is dominated by velocity dispersion, resulting in larger decomposition error.

We collect the velocity of the ionized gas traced by H α from the MaNGA DAP file (Westfall et al. 2019), which are represented by the grey squares in Fig. 5. The line-of-sight velocities of the secondary disc (blue circles) and the gas disc (grey squares) are totally consistent, indicating the secondary disc is co-rotating with the gas disc. Meanwhile, the primary disc (red circles) is counter-rotating with the gas disc. The fit on Ca II λ8542 lines in Figs 4(b) and (c) also provides velocities of two stellar discs in Regions A and B, which are shown as the crosses in Fig. 5, with the primary and secondary discs in red and blue, respectively. The line-of-sight velocities of the two stellar discs measured from Ca II λ8542 absorption lines match well with the results from the pPXF spectral decomposition.

3.2.3 *Orbit-based dynamical model*

The Schwarzschild orbit-superposition method (Schwarzschild 1979) is a powerful orbit-based dynamical modelling technique to reveal orbit structures in a galaxy. This method computes all possible stellar orbits in a given potential and assigns weight to each orbit to recover galaxy kinematics, including widely used parametric LOSVDs (e.g. Gaussian–Hermite expansion with velocity and velocity dispersion) in ordinary galaxies and non-parametric LOSVDs which are superior in describing the counter-rotating spectral features generated by two stellar discs. Compared with the spectral decomposition method, it uses spatial information contained in all IFS spectra of a galaxy and sidesteps the high SNR requirement when decomposing two stellar components directly from the spectra. In this section, we confirm the kinematics of the CRDs in SDSS J0748+4441 with the orbit-based dynamical models using the non-parametric LOSVDs of this galaxy.

We first extract the non-parametric LOSVDs of this galaxy from the MaNGA data cube with the BAYES-LOSVD package,[1] which employs Bayesian inference to obtain LOSVDs and the corresponding uncertainties. This package improves its efficiency by adopting a principal component analysis to reduce the requirement of stellar

[1] https://github.com/jfalconbarroso/BAYES-LOSVD

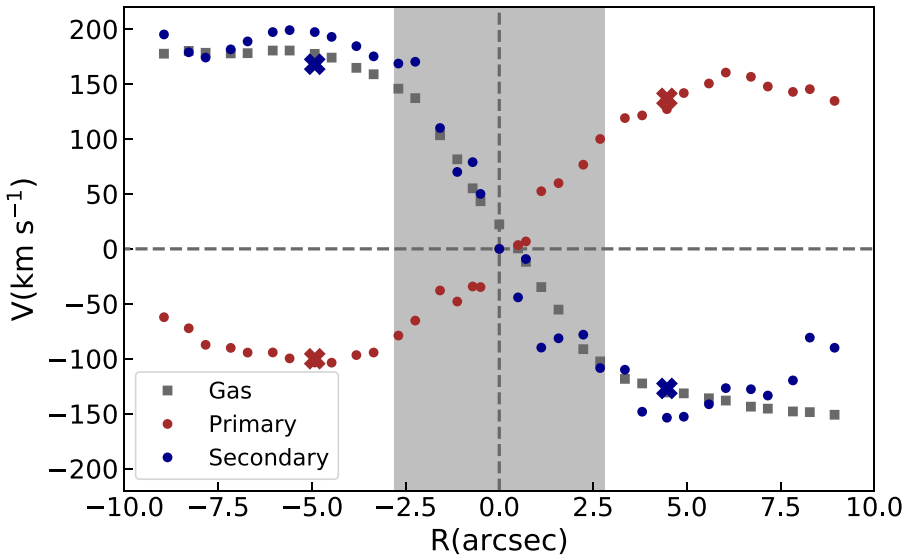

Figure 5. Line-of-sight velocities as functions of radii along the major axis. The circles represent the velocities from the pPXF spectral decomposition, with primary and secondary discs in red and blue. The red (primary disc) and blue (secondary disc) crosses represent the velocities from double Gaussian fit on Ca II λ8542. The grey squares represent the gas velocity traced by H α emission from the MaNGA DAP file.

templates, and provides several prior options to regularize the output LOSVDs. We refer readers to Falcón-Barroso & Martig (2021) for more details. For SDSS J0748+4441, the MaNGA spectra are first Voronoi binned to SNR > 50 using the median SNR within the fitting spectra range [4750, 5500] Å, and then fitted with the MILES stellar template library (Sánchez-Blázquez et al. 2006; Falcón-Barroso et al. 2011). The output LOSVDs have a velocity range $[-600, 600]$ km s^{-1} with a step of 30 km s^{-1} (∼1/2 MaNGA instrumental resolution). As an example, we show the LOSVD extraction of bin 130 in Fig. 6, which is the closest to the black-filled star in Fig. 4(a).

We then construct orbit-based dynamical models from the non-parametric LOSVDs using the DYNAMITE package (van den Bosch et al. 2008; Jethwa et al. 2020; Thater et al. 2022) and obtain the orbit distribution of this galaxy. We build the stellar mass distribution of this galaxy from its *r*-band image (Kaiser et al. 2002) with the MGE method (Emsellem, Monnet & Bacon 1994; Cappellari 2002). Moreover, we correct for its mass-to-light ratio with the stellar mass obtained from the data cube of PIPE3D (Sánchez et al. 2018), and introduce a variable to indicate the scale of the total stellar mass. We adopt the NFW dark matter profile described with virial mass M_{200} and concentration c. M_{200} is defined as the enclosed mass within the virial radius r_{200}, where the average density is 200 times the critical density ($\rho_{\rm crit} = 1.37 \times 10^{-7} {\rm M}_\odot$ pc^{-3}), and c is defined as the ratio of r_{200} to the scale radius of the NFW dark matter profile. We also include a central black hole with a fixed mass of 10^6 M$_\odot$. More details will be described in Yang et al. (in preparation). We show the fit along the major axis for SDSS J0748+4441 in Fig. 7, which includes bin 130 mentioned above.

We further characterize different orbit types with the circularity

$$\lambda_z = \overline{L_z}/r\overline{V_c}. \quad (1)$$

For each orbit, $\overline{L_z}$ is the mean angular momentum along the short axis, r is the average radius in equal time-step for each orbit, and $\overline{V_c}$ is the mean circular velocity (see equation 9 in Zhu et al. 2018a, for more detailed mathematical definitions). We divide the orbits into three stellar components by clear circularity distinctions at $\lambda_z = \pm 0.16$, shown as two blue dashed lines in the first panel of Fig. 8. The secondary disc is comprised of the co-rotating component classified as $\lambda_z > 0.16$, while the primary disc is comprised of the non-rotating and counter-rotating components classified as $-0.16 < \lambda_z < 0.16$ and $\lambda_z < -0.16$. In the second panel of Fig. 8, we display the line-of-sight orbital velocities as functions of radii along the top half of the major axis for the two stellar discs, with the primary and secondary discs represented by the orange and purple squares. The line-of-sight velocities obtained by the orbit-based model are consistent with those obtained by the spectral decomposition, with the primary and secondary discs represented by red and blue circles in the second panel of Fig. 8, respectively.

3.2.4 *Properties of two stellar discs*

Based on the disentangled spectra of the two stellar discs in SDSS J0748+4441, we compare the properties between them. We measure the Lick indices H β, Mgb, Fe5270, and Fe5335 (Worthey et al. 1994), for the primary and secondary components. H β can be used as an indicator of stellar population age. We also calculate the combined magnesium–iron index [MgFe]′ as $\sqrt{\rm Mgb \cdot (0.72 \cdot Fe5270 + 0.28 \cdot Fe5335)}$, which is independent of α-enhancement and can be an effective indicator of stellar metallicity (Thomas & Maraston 2003). Fig. 9(a) displays the H β indices as functions of [MgFe]′ indices along the major axis, with the primary and secondary discs in red and blue, respectively. The model-grid is the prediction from single stellar population models given by Thomas, Maraston & Johansson (2011). Comparing the data points with the model-grid, the secondary disc has younger stellar population and poorer stellar metallicity than the primary disc.

Fig. 9(b) displays the D$_n$4000 indices as functions of radii along the major axis. The circles represent the results from the pPXF two kinematic component fit, with the primary and secondary discs in red and blue, respectively. The stellar population of the primary disc is old, with D$_n$4000 of ∼1.8. Meanwhile, the stellar population of the secondary disc is young in the disc region, presenting a constant D$_n$4000 of ∼1.4. The D$_n$4000 of the secondary disc increases in the central region, where the emission is bulge-dominated.

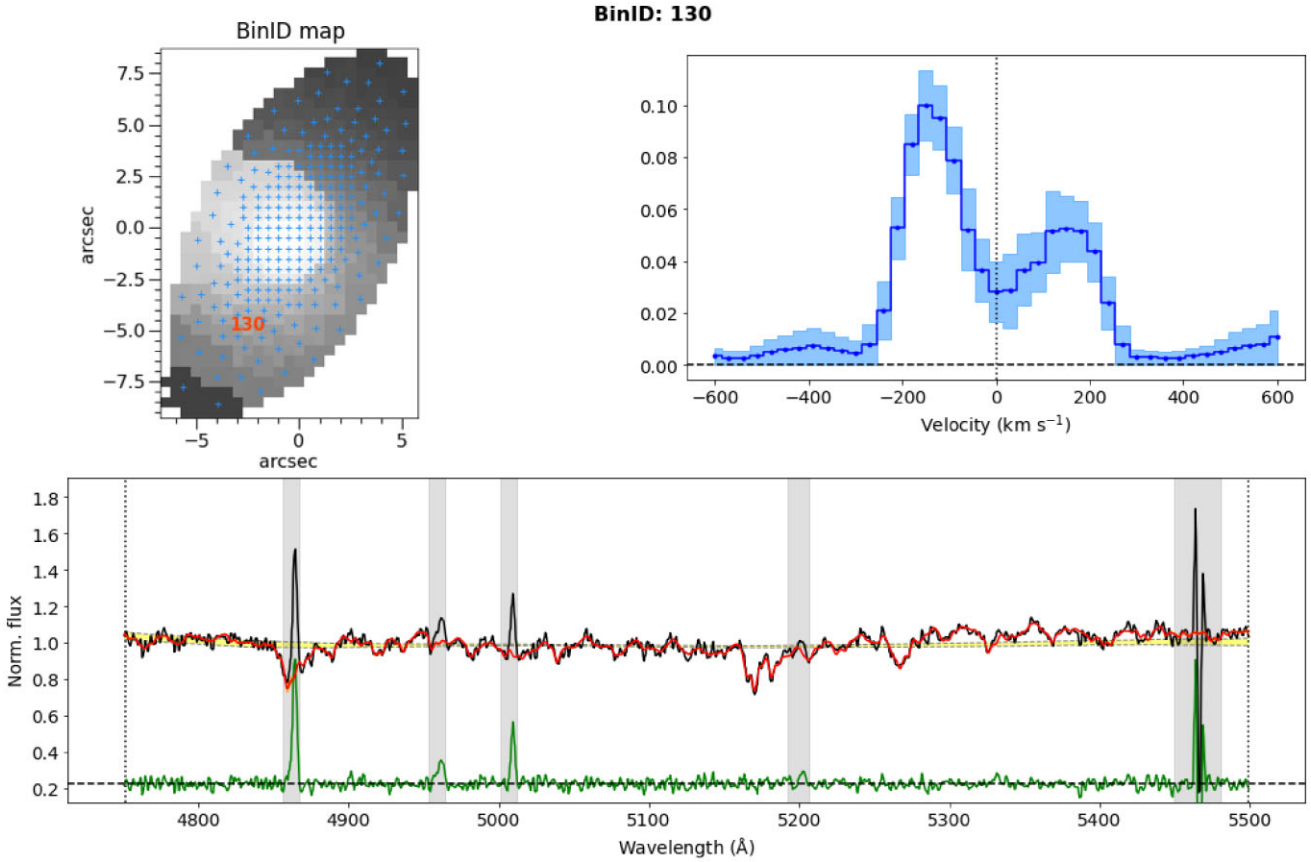

Figure 6. Spectra fit and LOSVD of bin 130 in orbit-based dynamical model generated by BAYES-LOSVD. Top left: the binning map with the position of bin 130 marked by the red id. Top right: the blue solid line and shadow are the LOSVD and $\pm 1\sigma$ error extracted by fitting the MaNGA spectra with BAYES-LOSVD. Bottom: MaNGA spectra (black), fit (red) and residual (green) of bin 130. The emission lines covered by the grey area are masked prior to fit.

Fig. 9(c) displays the stellar metallicity as functions of radii along the major axis, which is estimated by comparing the position of each circle with the model-grid in Fig. 9(a). The stellar metallicity of the primary disc is rich, and follows a constant distribution. Meanwhile, the stellar metallicity of the secondary disc is poor, and follows a negative gradient with metallicity decreasing on the outskirts. Given the bulge-dominated feature in the central region displayed in Fig. 9(b), we do not overinterpret the negative gradient here. Moreover, we estimate the stellar population age for two stellar discs in Fig. 9(a), and find the stellar population of the primary disc being older than that of the secondary disc, which is consistent with the D_n4000 indices in Fig. 9(b).

4 FORMATION OF CRDS IN SDSS J0748+4441

Early studies proposed that internal structures such as bulge and bar (Evans & Collett 1994) are responsible for the formation of CRDs. However, these scenarios failed to explain the presence of different stellar populations of two stellar discs (Coccato et al. 2013), which instead can be the results of external processes such as mergers and gas accretion (Corsini 2014). Major merger is known to be a destructive event that heats the system significantly, destroys the morphology of galaxies, and results in the formation of an elliptical galaxy. On the other hand, gas-rich minor merger and gas accretion are milder processes delivering the external gas that is counter-rotating with the pre-existing gas, and have weaker influence on the galaxy morphology (Bournaud, Jog & Combes 2005).

With the development of long-slit spectroscopic and IFS instruments, studies on both individual galaxies (Coccato et al. 2011; Johnston et al. 2013) and galaxy samples (Bao et al. 2022; Bevacqua, Cappellari & Pellegrini 2022) confirmed that the external processes including mergers and gas accretion contribute to the formation of CRDs. The common point in these processes is that the lately forming stellar disc inherits the angular momentum from the external gas, which is counter-rotating with the pre-existing stellar disc. During the formation of CRDs, once the external gas with opposite direction is abundant enough to dominate the gas rotation, the misalignment between gas and stars will be observed in galactic scale (Chen et al. 2016; Xu et al. 2022). Davis et al. (2011) found that the gas and stars are misaligned in ∼42 per cent early-type galaxies in ATLAS^{3D}. However, assuming mergers as the only source of misalignment in simulation, Lagos et al. (2015) obtained only ∼2–5 per cent early-type galaxies with misaligned gas and stars. After adding gas accretion in their simulation, the misalignment between gas and stars was found in ∼46 per cent early-type galaxies. These studies proved that gas accretion is a key process of bringing the external gas with opposite direction.

Based on the pPXF two kinematic component fit as displayed in Fig. 4(d), we calculate the flux contributions of two stellar discs in each spaxel. Fig. 10(a) displays the flux contributions as functions of radii along the major axis, with the primary and secondary discs in red and blue, respectively. The primary disc is more luminous than the secondary disc across the whole galaxy. The average flux ratio between the primary and secondary discs is ∼1.8. We also estimate

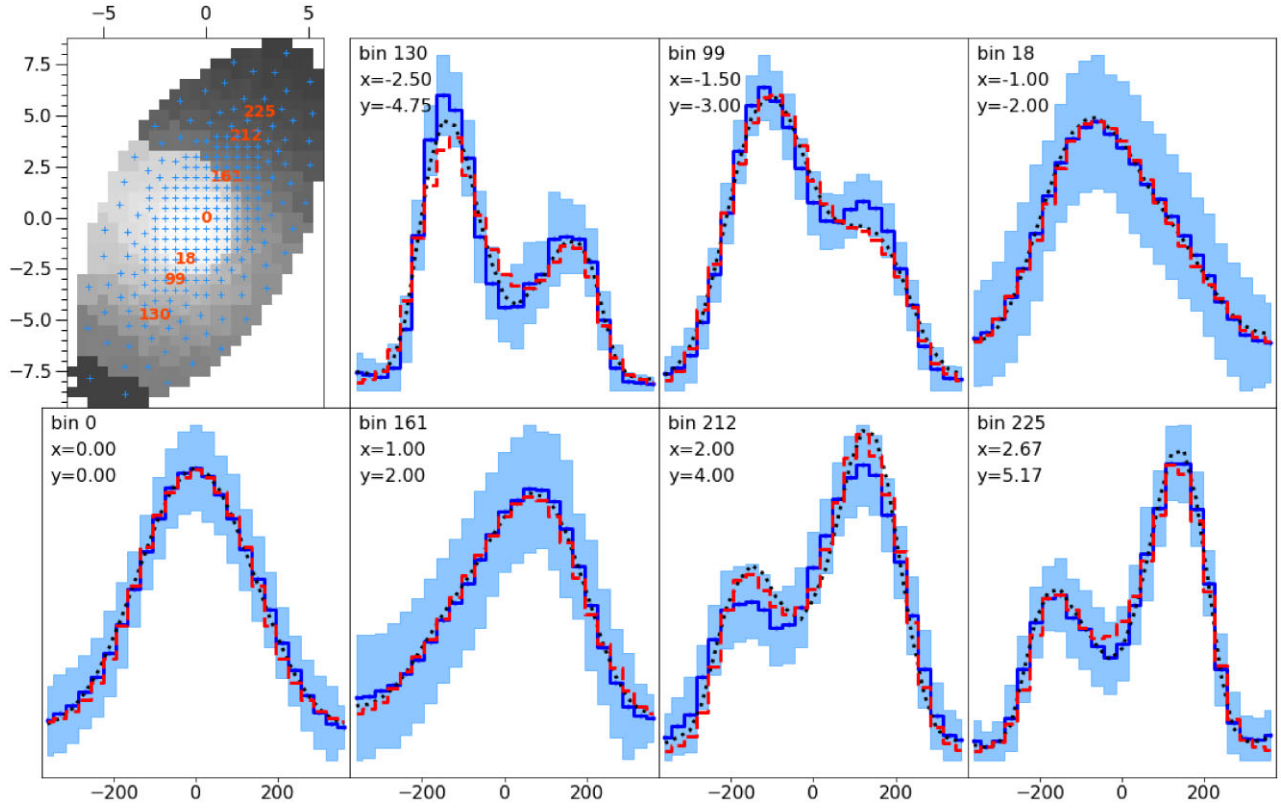

Figure 7. Fitting LOSVD along the major axis in orbit-based dynamical model. First panel: the binning map showing the ids and positions (in arcsec) of all the bins shown in the following panels. Other panels: the blue solid line and shadow are the LOSVD and $\pm 1\sigma$ error obtained with BAYES-LOSVD, the red dashed line are the best-fitting model, and the black dotted line are the symmetrized data for comparison because the model is axis-symmetric.

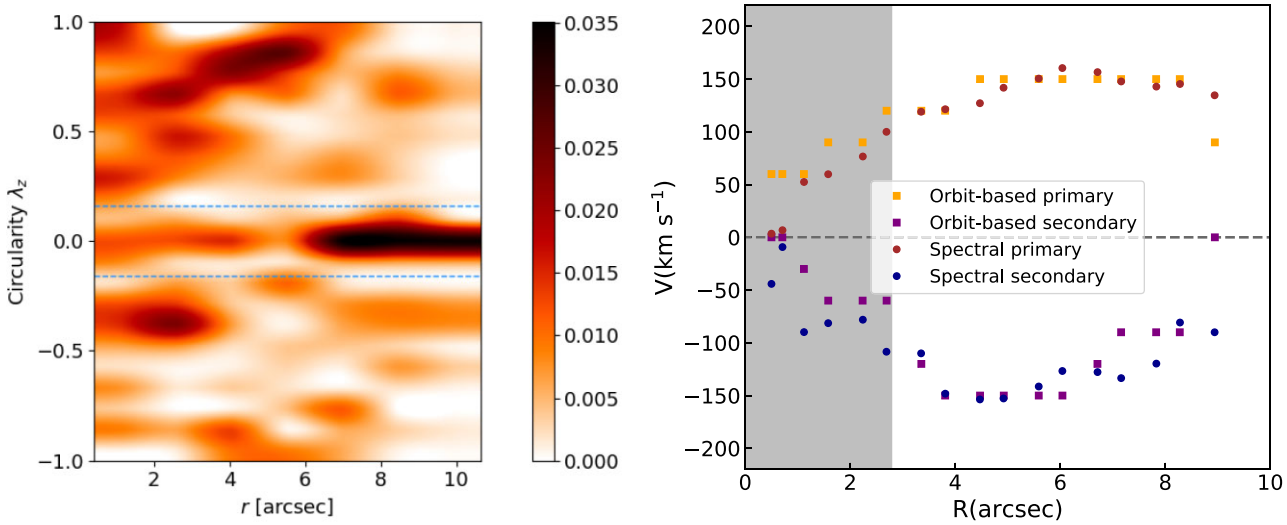

Figure 8. Best-fitting orbit-based dynamical model on the phase-space and the resulting line-of-sight velocities. First panel: The probability density of stellar orbits on the phase-space of circularity λ_z versus average radius r of the best-fitting model. The blue dashed lines indicate $\lambda_z = \pm 0.16$. The colourbar shows the probability density of orbits. Second panel: The red and blue circles are the same as Fig. 5. The squares represent the velocities from the orbit-based dynamical model, with primary and secondary discs in orange and purple.

the masses of two stellar discs based on the decomposed spectra. For each disc model, we convolve the model spectrum with the SDSS u, g, r, i, z filters to get the AB magnitudes. The stellar mass-to-light ratio is then obtained by comparing the u, g, r, i, z magnitudes of each stellar disc with mimic galaxies generated in Chen et al. (2012). We refer readers to Chen et al. (2012) for more details of the methodology. Fig. 10(b) displays the stellar masses of two stellar discs as functions of radii, with the primary and secondary discs in

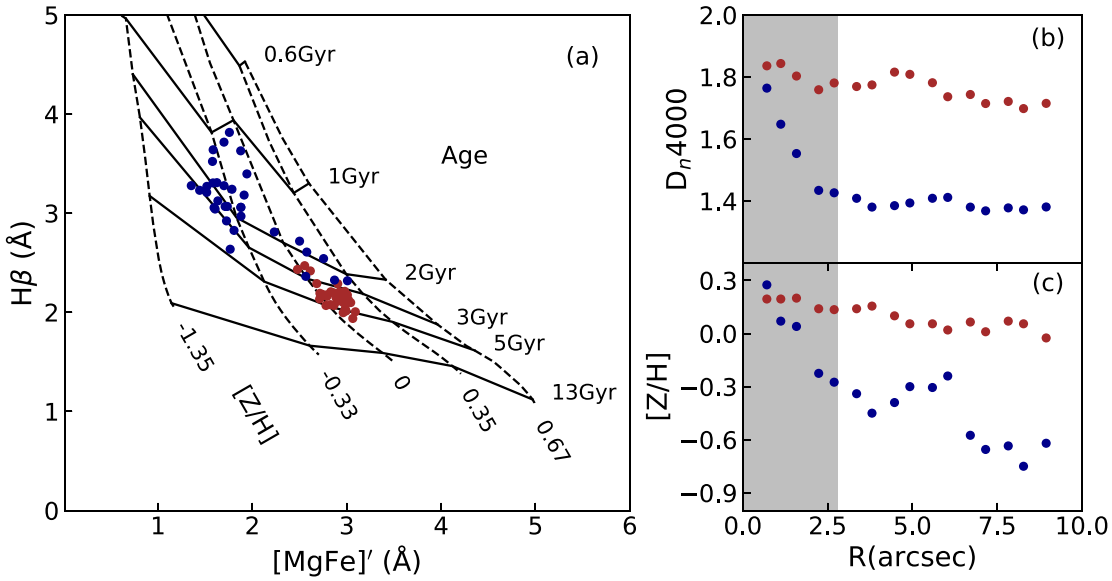

Figure 9. Properties of two stellar discs along the major axis. (a) The circles show H β indices as functions of [MgFe]′ indices, with the primary and secondary discs in red and blue. The model-grid is the prediction from single stellar population models given by Thomas, Maraston & Johansson (2011). (b) and (c) The circles show the D_n4000 indices and stellar metallicity as functions of radii, with the primary and secondary discs in red and blue.

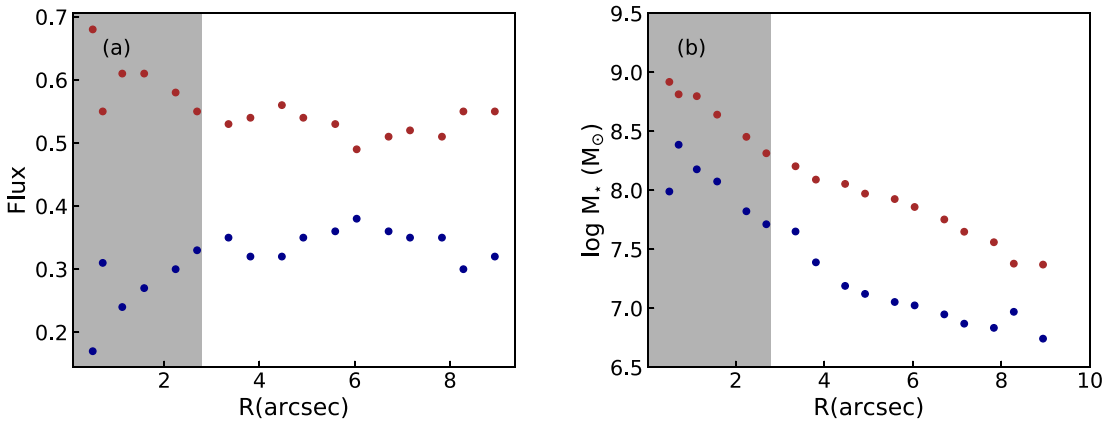

Figure 10. Contributions of two stellar discs along the major axis. (a) and (b) The circles show the fluxes and stellar masses as functions of radii, with the primary and secondary discs in red and blue.

red and blue, respectively. The primary disc is more massive than the secondary disc across the whole galaxy, with mass ratio of ∼5.2.

A gas-rich minor merger in retrograde orbit can provide abundant gas that is counter-rotating with the pre-existing stars, and fuel the formation of secondary disc. Ji, Peirani & Yi (2014) simulated mergers with different mass ratios, and found that the merger remnant features can be observed for ∼5.8 Gyr at *r*-band magnitude limit of ∼25 mag arcsec^{-2} for a merger with a mass ratio of 6. The stellar population age of the secondary disc in SDSS J0748+4441 is ∼2 Gyr in Fig. 9(b), suggesting that the gas-rich minor merger should happen ∼2 Gyr ago. On the other hand, the DESI *g*, *r*, *z* colour image (Dey et al. 2019) of SDSS J0748+4441 is displayed in Fig. 1(d), which is much deeper than 25 mag arcsec^{-2} in *r* band. We follow the method described in Li et al. (2021) to check whether there is any merger remnant feature, finding that it is an isolated galaxy. The gas-rich minor merger is inapplicable to explain the formation of CRDs in SDSS J0748+4441 due to the lack of merger remnant features.

We propose gas accretion in retrograde orbit as formation scenario for CRDs in SDSS J0748+4441. Given the stellar population age of the secondary disc in Fig. 9(b), the gas accretion in this galaxy happened ∼2 Gyr ago. The global stellar mass of this galaxy in the MaNGA DRP is $\sim 10^{10}$ $M_\odot$. Combining the mass ratio of ∼5.2 between two stellar discs (Fig. 10b), accretion brought at least 1.6×10^9 $M_\odot$ counter-rotating gas into SDSS J0748+4441. The gas accretion can originate from galaxy environment including the cosmic web (Katkov et al. 2016) or a gas-rich companion (Coccato et al. 2011).

ACKNOWLEDGEMENTS

We are grateful to Can Xu for her valuable comments. MB acknowledges support from the National Natural Science Foundation of China, NSFC Grant No. 12303009. YC acknowledges support from the National Natural Science Foundation of China, NSFC Grant

Nos. 12333002, 11573013, 11733002, 11922302, the China Manned Space Project with NO. CMS-CSST-2021-A05. MY acknowledges support from the China Postdoctoral Science Foundation, Grant No. 2021M703337. This work was supported by the research grants from the China Manned Space Project, the second-stage CSST science project 'Investigation of small-scale structures in galaxies and forecasting of observations'.

Funding for the Sloan Digital Sky Survey IV has been provided by the Alfred P. Sloan Foundation, the U.S. Department of Energy Office of Science, and the Participating Institutions. SDSS- IV acknowledges support and resources from the Center for High-Performance Computing at the University of Utah. The SDSS web site is www.sdss.org. SDSS-IV is managed by the Astrophysical Research Consortium for the Participating Institutions of the SDSS Collaboration including the Brazilian Participation Group, the Carnegie Institution for Science, Carnegie Mellon University, the Chilean Participation Group, the French Participation Group, Harvard-Smithsonian Center for Astrophysics, Instituto de Astrofísica de Canarias, The Johns Hopkins University, Kavli Institute for the Physics and Mathematics of the Universe (IPMU) / University of Tokyo, Lawrence Berkeley National Laboratory, Leibniz Institut für Astrophysik Potsdam (AIP), Max-Planck-Institut für Astronomie (MPIA Heidelberg), Max-Planck-Institut für Astrophysik (MPA Garching), Max-Planck-Institut für Extraterrestrische Physik (MPE), National Astronomical Observatory of China, New Mexico State University, New York University, University of Notre Dame, Observatório Nacional / MCTI, The Ohio State University, Pennsylvania State University, Shanghai Astronomical Observatory, United Kingdom Participation Group, Universidad Nacional Autónoma de México, University of Arizona, University of Colorado Boulder, University of Oxford, University of Portsmouth, University of Utah, University of Virginia, University of Washington, University of Wisconsin, Vanderbilt University, and Yale University.

DATA AVAILABILITY

The data underlying this article will be shared on reasonable request to the corresponding author.

REFERENCES

Baldwin J. A., Phillips M. M., Terlevich R., 1981, PASP, 93, 5
Bao M. et al., 2022, ApJ, 926, L13
Bevacqua D., Cappellari M., Pellegrini S., 2022, MNRAS, 511, 139
Blanton M. R. et al., 2017, AJ, 154, 28
Bournaud F., Jog C. J., Combes F., 2005, A&A, 437, 69
Bundy K. et al., 2015, ApJ, 798, 7
Cappellari M., 2002, MNRAS, 333, 400
Cappellari M., 2017, MNRAS, 466, 798
Chen Y.-M. et al., 2012, MNRAS, 421, 314
Chen Y.-M. et al., 2016, Nat. Commun., 7, 13269
Coccato L., Morelli L., Corsini E. M., Buson L., Pizzella A., Vergani D., Bertola F., 2011, MNRAS, 412, L113
Coccato L., Morelli L., Pizzella A., Corsini E. M., Buson L. M., Dalla Bontà E., 2013, A&A, 549, A3
Corsini E. M., 2014, in Iodice E., Corsini E. M., eds, ASP Conf. Ser. Vol. 486, Multi-Spin Galaxies. Astron. Soc. Pac., San Francisco, p. 51
Davis T. A. et al., 2011, MNRAS, 414, 968
Dey A. et al., 2019, AJ, 157, 168
Ding Y. et al., 2023, A&A, 672, A84
Emsellem E., Monnet G., Bacon R., 1994, A&A, 285, 723
Evans N. W., Collett J. L., 1994, ApJ, 420, L67
Falcón-Barroso J., Martig M., 2021, A&A, 646, A31
Falcón-Barroso J., Sánchez-Blázquez P., Vazdekis A., Ricciardelli E., Cardiel N., Cenarro A. J., Gorgas J., Peletier R. F., 2011, A&A, 532, A95
Gunn J. E. et al., 2006, AJ, 131, 2332
Jethwa P., Thater S., Maindl T., Van de Ven G., 2020, Astrophysics Source Code Library, record ascl:2011.007
Ji I., Peirani S., Yi S. K., 2014, A&A, 566, A97
Jin Y., Zhu L., Long R. J., Mao S., Wang L., van de Ven G., 2020, MNRAS, 491, 1690
Johnston E. J., Merrifield M. R., Aragón-Salamanca A., Cappellari M., 2013, MNRAS, 428, 1296
Kaiser N. et al., 2002, in Anthony T. J., Sidney W., eds, Proc. SPIE Conf. Ser. Vol. 4836, Survey and Other Telescope Technologies and Discoveries. SPIE, Bellingham, p. 154
Katkov I. Y., Sil'chenko O. K., Chilingarian I. V., Uklein R. I., Egorov O. V., 2016, MNRAS, 461, 2068
Katkov I., Chilingarian I., Sil'chenko O., Zasov A., Afanasiev V., 2011, Balt. Astron., 20, 453
Kauffmann G. et al., 2003, MNRAS, 346, 1055
Kewley L. J., Dopita M. A., Sutherland R. S., Heisler C. A., Trevena J., 2001, ApJ, 556, 121
Krajnović D., Cappellari M., de Zeeuw P. T., Copin Y., 2006, MNRAS, 366, 787
Krajnović D. et al., 2011, MNRAS, 414, 2923
Lagos C. del P., Padilla N. D., Davis T. A., Lacey C. G., Baugh C. M., Gonzalez-Perez V., Zwaan M. A., Contreras S., 2015, MNRAS, 448, 1271
Law D. R. et al., 2016, AJ, 152, 83
Li S.-L. et al., 2021, MNRAS, 501, 14
Mitzkus M., Cappellari M., Walcher C. J., 2017, MNRAS, 464, 4789
Pizzella A., Morelli L., Corsini E. M., Dalla Bontà E., Coccato L., Sanjana G., 2014, A&A, 570, A79
Pizzella A., Morelli L., Coccato L., Corsini E. M., Dalla Bontà E., Fabricius M., Saglia R. P., 2018, A&A, 616, A22
Rix H.-W., Franx M., Fisher D., Illingworth G., 1992, ApJ, 400, L5
Rubin V. C., Graham J. A., Kenney J. D. P., 1992, ApJ, 394, L9
Rubino M., Pizzella A., Morelli L., Coccato L., Portaluri E., Debattista V. P., Corsini E. M., Dalla Bontà E., 2021, A&A, 654, A30
Sánchez S. F. et al., 2016, Rev. Mex. Astron. Astrofis., 52, 21
Sánchez S. F. et al., 2018, Rev. Mex. Astron. Astrofis., 54, 217
Sánchez-Blázquez P. et al., 2006, MNRAS, 371, 703
Santucci G. et al., 2022, ApJ, 930, 153
Schwarzschild M., 1979, ApJ, 232, 236
Smee S. A. et al., 2013, AJ, 146, 32
Tahmasebzadeh B., Zhu L., Shen J., Gerhard O., van de Ven G., 2022, ApJ, 941, 109
Thater S. et al., 2022, A&A, 667, A51
Thomas D., Maraston C., 2003, A&A, 401, 429
Thomas D., Maraston C., Johansson J., 2011, MNRAS, 412, 2183
van den Bosch R. C. E., van de Ven G., Verolme E. K., Cappellari M., de Zeeuw P. T., 2008, MNRAS, 385, 647
Westfall K. B. et al., 2019, AJ, 158, 231
Worthey G., Faber S. M., Gonzalez J. J., Burstein D., 1994, ApJS, 94, 687
Xu H. et al., 2022, MNRAS, 511, 4685
Zhu L. et al., 2018a, MNRAS, 473, 3000
Zhu L., van de Ven G., Méndez-Abreu J., Obreja A., 2018b, MNRAS, 479, 945

This paper has been typeset from a TEX/LATEX file prepared by the author.